

## Self-Assembly

International Edition: DOI: 10.1002/anie.201807776  
German Edition: DOI: 10.1002/ange.201807776

## Design Rules for Self-Assembly of 2D Nanocrystal/Metal–Organic Framework Superstructures

Fen Qiu, John R. Edison, Zdenek Preisler, Yan-Fang Zhang, Guo Li, Aizhao Pan, Chih-Hao Hsu, Tracy M. Mattox, Peter Ercius, Chengyu Song, Karen Bustillo, Michael A. Brady, Edmond W. Zaia, Sohee Jeong, Jeffrey B. Neaton, Shixuan Du, Stephen Whitelam, and Jeffrey J. Urban\*

**Abstract:** We demonstrate the guiding principles behind simple two dimensional self-assembly of MOF nanoparticles (NPs) and oleic acid capped iron oxide ( $\text{Fe}_3\text{O}_4$ ) NCs into a uniform two-dimensional bi-layered superstructure. This self-assembly process can be controlled by the energy of ligand–ligand interactions between surface ligands on  $\text{Fe}_3\text{O}_4$  NCs and  $\text{Zr}_6\text{O}_4(\text{OH})_4(\text{fumarate})_6$  MOF NPs. Scanning transmission electron microscopy (TEM)/energy-dispersive X-ray spectroscopy and TEM tomography confirm the hierarchical co-assembly of  $\text{Fe}_3\text{O}_4$  NCs with MOF NPs as ligand energies are manipulated to promote facile diffusion of the smaller NCs. First-principles calculations and event-driven molecular dynamics simulations indicate that the observed patterns are dictated by combination of ligand–surface and ligand–ligand interactions. This study opens a new avenue for design and self-assembly of MOFs and NCs into high surface area assemblies, mimicking the structure of supported catalyst architectures, and provides a thorough fundamental understanding of the self-assembly process, which could be a guide for designing functional materials with desired structure.

**D**imensionally controlled inorganic nanocrystals (NCs) and metal organic frameworks (MOF) are two powerful fields of materials science, each providing new approaches to energy storage, conversion, and catalysis.<sup>[1,2]</sup> However, the promise of uniting the complementary functions of these two materials into hybrid assemblies exhibiting enhanced gas storage or

catalytic behavior has not been realized because of a lack of synthetic control over essential NC–MOF interfaces. Currently, the only hybrid assemblies reported are variants on a core–shell or controlled encapsulation scheme, and no general rules of design exist that govern co-assembly or synthesis.<sup>[3]</sup> Therefore, these ad hoc approaches are intrinsically limited and also critically sacrifice the performance of the materials for transport and catalysis due to the encapsulated topology. The engineering of nanoparticles (NPs) into well-defined superstructures has enabled new insight into the processes of self-assembly and also opened technological applications in electronics,<sup>[4]</sup> optics,<sup>[5]</sup> catalysis<sup>[2,6]</sup> and biomedicine.<sup>[7]</sup> Spatially organized combinations of various types of semiconductors, metals and magnetic nanoparticles have led to the emergence of novel collective properties of the superstructured assemblies through a close interaction between different components in ordered geometries.<sup>[8–12]</sup> In general, the formation of highly ordered superlattices via spontaneous self-assembly of colloidal inorganic NCs is governed by entropic and energetic interactions.<sup>[13,14]</sup> However, merely mixing different types of NPs together seldom leads to self-assembly of ordered structures, and often results in uncontrolled phase segregation. In addition to tuned interactions, excellent size and shape uniformity of the NPs is required to obtain ordered geometries.<sup>[15,16]</sup> This proves to be a significant challenge especially for nanoparticles made from metal organic frameworks (MOF), given that their size and morphology are difficult to control. Fortunately, one can take advantage of ligand interactions to optimize the self-assembly. This concept has been demonstrated in the field of NC–DNA assemblies, where ligand interaction is the main driving force and the NPs become decorations on the DNA scaffold.<sup>[17]</sup>

At present, a handful of groups have begun to identify ways to fabricate MOF in order to harness their potential utilities.<sup>[18]</sup> MOF are comprised of a high surface area porous organic skeleton with programmable pendant chemical groups as linkers that connect open metal sites. Their structure suggests that MOF containing materials could be specifically designed for catalysis applications.<sup>[19–22]</sup> Thus, MOFs have been recognized as a promising candidate to become superstructure building blocks with desired functionalities. In addition, iron oxide ( $\text{Fe}_3\text{O}_4$ ) NCs are widely used for catalysis and electrochemical energy storage, and are amongst the most common building blocks for controlled self-assembly

[\*] F. Qiu, J. R. Edison, Z. Preisler, G. Li, A. Pan, C.-H. Hsu, T. M. Mattox, E. W. Zaia, S. Jeong, J. B. Neaton, S. Whitelam, J. J. Urban  
The Molecular Foundry, Lawrence Berkeley National Laboratory  
1 Cyclotron Road, Berkeley, CA 94720 (USA)  
E-mail: jjurban@lbl.gov

Y.-F. Zhang, S. Du  
Institute of Physics & University of Chinese Academy of Sciences,  
Chinese Academy of Sciences  
Beijing 100190 (China)

P. Ercius, C. Song, K. Bustillo  
National Center for Electron Microscopy, The Molecular Foundry,  
Lawrence Berkeley National Laboratory  
Berkeley, CA 94720 (USA)

M. A. Brady  
Advanced Light Source, Lawrence Berkeley National Laboratory  
Berkeley, CA 94720 (USA)

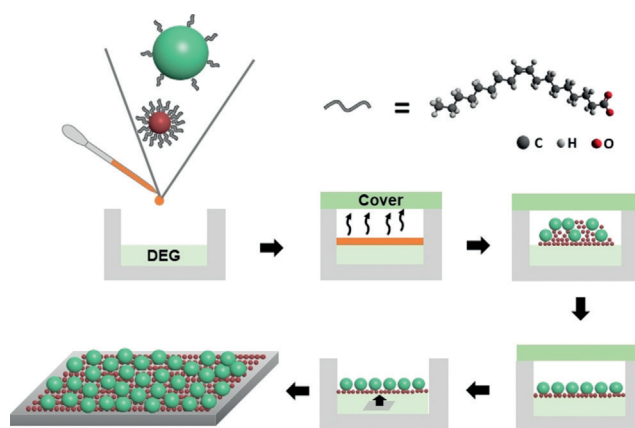
Supporting information and the ORCID identification number(s) for the author(s) of this article can be found under <https://doi.org/10.1002/anie.201807776>.

because of their narrow size distribution achieved by large-scale colloidal synthesis.

In this study, we demonstrate self-assembly of MOF NPs with inorganic  $\text{Fe}_3\text{O}_4$  NCs, breaking conventional wisdom limiting the size and morphology uniformity required for building blocks to be assembled into superstructures. Compared to the state of art colloidal self-assembly of NPs into ordered arrays which generally required narrow size distribution and well controlled the surface ligands of the NPs, we broke the limitation of strict control on size and surface ligands, and intimated using MOF into self-assembly. Compared to state-of-the-art colloidal self-assembly of inorganic semiconductor NPs into binary superlattices, which generally requires narrow size distributions and well-controlled surface ligands of the NPs, we introduce new methods that relax these strict limitations of particle control on size and surface ligands, enabling us to integrate MOF particles into self-assembled superstructures. We firstly achieved a  $\text{Fe}_3\text{O}_4$ -MOF NP bilayer superstructure, producing a uniform film with precise NP packing and rigorous control on the interparticle distance. For the purpose of designing supported catalyst architectures during the self-assembly process, the achieved long-range hexagonal ordered OA capped  $\text{Fe}_3\text{O}_4$  superlattice worked as a supporting template for helping a single layered MOF film sitting on its top, forming a 2D bi-layered superstructure. While polystyrene (PS) capped  $\text{Fe}_3\text{O}_4$  randomly mix with MOF NPs into the same plane and form a mixed monolayer. First principles calculations and event-driven molecular dynamics (MD) simulations were used to understand the different self-assembly behaviors. Based on the interaction energies calculated from density functional theory, the self-assembly behaviors were simulated using the MD method. Our experimental observations along with theoretical modeling and simulations have together proved a more in-depth understanding of these complicated self-assembly processes. This study initiated MOF-based self-assembly, opening a new avenue for using MOFs as solution processing building blocks for co-assembling with other types of materials into intricate superstructures. In addition, the bilayered superstructures mimic well-known supported catalyst architectures, with extended advantages of enabling detailed modulation of the composition and interface of the MOF NPs and iron oxide supports.<sup>[23]</sup>

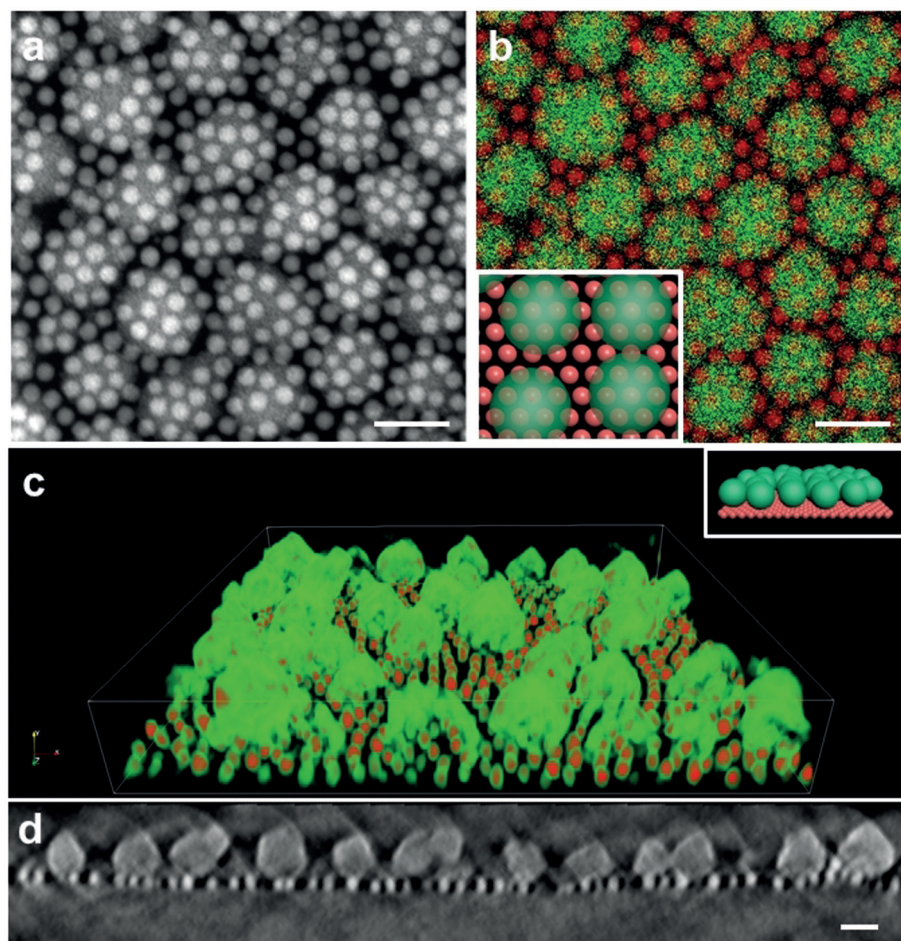
We adapted the air-liquid interface assembly method to the co-self-assembly of MOF NPs with inorganic  $\text{Fe}_3\text{O}_4$  NCs (Scheme 1).<sup>[24]</sup> This method has been generally used for forming binary inorganic NC superlattices, and we adapted this method to form the  $\text{Fe}_3\text{O}_4$ -MOF superstructures in our studies (details of the process are in the Supporting Information). In our binary system,  $\approx 50$  nm diameter  $\text{Zr}_6\text{O}_4(\text{OH})_4(\text{fumarate})_6$  MOF NPs are assembled with  $\approx 12$  nm diameter inorganic  $\text{Fe}_3\text{O}_4$  NCs with the size ration 4:1, which is the largest size difference reported between two NPs used for self-assembly.

Figure 1a shows a representative scanning transmission electron microscopy (STEM) image of the superstructure self-assembled from oleic acid capped  $\text{Fe}_3\text{O}_4$  (OA- $\text{Fe}_3\text{O}_4$ ) and OA capped MOF NPs, clearly revealing that the two sets of NPs uniformly integrate into different layers. It also suggests



**Scheme 1.** Cartoon of the 2D bi-layered superstructure film growth and transfer processes. Red sphere =  $\text{Fe}_3\text{O}_4$  NCs, green sphere = MOF NPs.

that the OA- $\text{Fe}_3\text{O}_4$  NCs form locally ordered hexagonal superlattices while the MOF NPs maintain uniform packing into one single layer. Elemental mapping using energy-dispersive X-ray spectroscopy (EDX) confirmed each component in the system was either a MOF containing Zr or a  $\text{Fe}_3\text{O}_4$  NC represented by the Fe element (Figure 1b). However, the lateral structure of the co-assembly was still ambiguous, as the projection images cannot distinguish between two possible structures: i.  $\text{Fe}_3\text{O}_4$  and MOF as separated layers; ii.  $\text{Fe}_3\text{O}_4$  covers the surface of the MOF. In order to understand how the two types of NPs co-assembled in the lateral plane, three-dimensional (3D) transmission electron microscopy tomographic images were acquired. The tilt series were fed into an iterative tomographic reconstruction to obtain a three-dimensional rendering of the superstructure, showing the bi-layered superstructure system (Figure 1c). The image of the cross-section achieved after reconstruction confirms that the MOF NPs formed a single layer on top of a mono-layered  $\text{Fe}_3\text{O}_4$  NC superlattice (Figure 1d). A 3D 360° rendering provided a vivid animation (Supporting Information) showing the excellent uniformity of the bi-layered superstructure. In this binary system, the layer of  $\text{Fe}_3\text{O}_4$  NP superlattice is closely connected to MOF layer, suggesting a powerful approach for designing a supported catalyst. In order to understand the uniformity of the binary system, the average interparticle distance between OA- $\text{Fe}_3\text{O}_4$  NPs was measured to be 14.5 nm (Figure S1), which is consistent with the interparticle distance of the single component superlattice of OA- $\text{Fe}_3\text{O}_4$  NPs measured from TEM images (Figure S2). In addition, the measured interparticle distance between MOF NPs in this bi-layered superstructure is  $58 \pm 15$  nm, suggesting a high degree of uniformity in the nanostructured bi-layer (Figure S1). In this self-assembly process, although the size of the MOF NP is not uniform, the achieved long-range hexagonal ordered OA capped  $\text{Fe}_3\text{O}_4$  superlattice worked as a supporting template to facilitate a single layer MOF film sitting on its top surface, forming a 2D bi-layered superstructure. The monolayer of MOF on top of the  $\text{Fe}_3\text{O}_4$  NP superlattice is more uniform, compared to the single component MOF film (Figure S3) which suggests that there is an interaction between the two



**Figure 1.** TEM images of self-assembled NC-MOF bi-layered superstructure. a) STEM image of the 2D bi-layered superstructure film (scale bar is 50 nm). b) STEM/EDX confirm the element of each NPs (red is Fe-K $\alpha$  and green is the sum of Zr-K $\alpha$  and Zr-L $\alpha$ , scale bar is 50 nm). The inset shows cartoon mimicking the top-down image (c) Slice from the 3D tomography reconstruction. The color scale is only as a guide to the reader for ease, red corresponds to Fe representing Fe<sub>3</sub>O<sub>4</sub> NCs, green corresponds to Zr representing MOF NPs. The inset shows cartoon mimicking the cross-section image (d) Cross-section TEM image of 2D bi-layered superstructure film by a tilt tomography reconstruction (scale bar is 70 nm).

layers of NPs. It should be noted that there are areas where the single component MOF assembly or Fe<sub>3</sub>O<sub>4</sub> assembly co-existed and mixed with the bi-layered superstructures, but the majority of the area showed a uniform MOF-Fe<sub>3</sub>O<sub>4</sub> bi-layered superstructure. It should also be noted that the 2D bi-layered superstructure was observed when the concentration of Fe<sub>3</sub>O<sub>4</sub> was larger than MOF in the mixed solution of the assembly process. This promotes the hypothesis that the Fe<sub>3</sub>O<sub>4</sub> NP superlattice might assemble at the bottom due to the ligand-surface interaction.

From the above discussion, when the droplet of solution is released in the air-liquid interface during self-assembly, the large numbers of OA-Fe<sub>3</sub>O<sub>4</sub> NCs form a large area of compact superlattice while MOF NPs do not have space to insert into the Fe<sub>3</sub>O<sub>4</sub> NC superlattice plane. Thus, the MOF NPs sit on top of the Fe<sub>3</sub>O<sub>4</sub> layer. The uniform bi-layered superstructure area can be as large as 1  $\mu\text{m}$  as shown in Figure 2a. In order to study how the energetic interaction influences the self-

assembly, the surface ligands of Fe<sub>3</sub>O<sub>4</sub> were changed from OA to polystyrene (PS), a grafted polymer with higher molecular weight while retaining softness and strong ligand-ligand interactions, which leads to change of the energetic interaction in the diffusion rate definition based on Fick's first law. Under the same self-assembly condition for assembling PS-Fe<sub>3</sub>O<sub>4</sub> NCs with MOF NPs (details in the Supporting Information), we observed that PS-Fe<sub>3</sub>O<sub>4</sub> NCs were separated by MOF NPs in the same plane, and the bigger MOF NPs were surrounded by smaller PS-Fe<sub>3</sub>O<sub>4</sub> NCs (Figure 2b), indicating a simultaneous diffusion of the two types of NPs to form a single layer. Resonant soft X-ray scattering (RSXS) showed a hexagonal order corresponding to the superlattice layer of Fe<sub>3</sub>O<sub>4</sub> formed in both samples, but the X-ray intensity was higher in the OA-Fe<sub>3</sub>O<sub>4</sub>-MOF system (Figure S4). The higher *x*-ray intensity in the OA-Fe<sub>3</sub>O<sub>4</sub>-MOF sample indicates more hexagonal order area in the bi-layer superstructures; in the PS-Fe<sub>3</sub>O<sub>4</sub> and MOF system, insertion of MOF into the Fe<sub>3</sub>O<sub>4</sub> superlattice plane leads to less hexagonal order. The largest Fe<sub>3</sub>O<sub>4</sub> NC spacing was measured to be 13.05 nm when the surface organic ligand is OA as

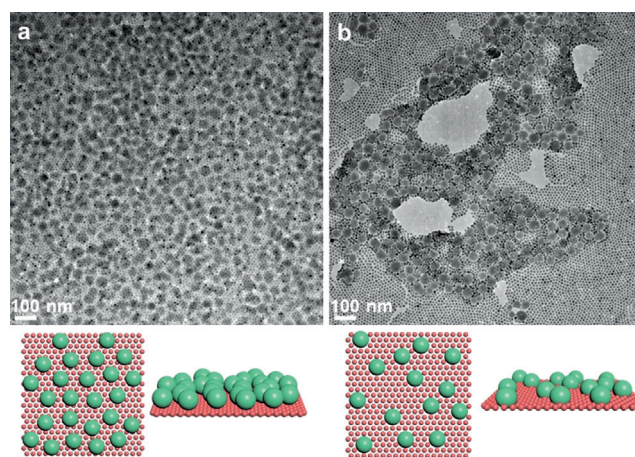


**Figure 2.** TEM images of films co-assembled by MOF and Fe<sub>3</sub>O<sub>4</sub> NCs with different ligands. a) is with OA as ligands. b) is with PS as ligands. The cartoons illustrate the self-assembly of two processes due to the different surface ligands of Fe<sub>3</sub>O<sub>4</sub> NCs representing TEM images above, respectively: red sphere = Fe<sub>3</sub>O<sub>4</sub> NCs, green sphere = MOF NPs.

compared to 13.27 nm when the surface organic ligand is PS. This increased inter-particle distance in the PS-Fe<sub>3</sub>O<sub>4</sub> NC superlattice after ligand exchange is significant and consistent with the FFT calculations, indicating that the PS ligand is longer than OA capping on the surface of the Fe<sub>3</sub>O<sub>4</sub> NCs. The absolute value is different from the FFT measurements most likely because of the larger average area (200 μm) illuminated by RSoXS and because of the different substrates used for these two measurements.

In our systems, the two different assembly processes are only distinguished by the surface ligands of Fe<sub>3</sub>O<sub>4</sub> NCs, which mainly contribute to the energetic interactions in the co-assembly process. To understand this phenomenon, we performed First Principles Calculations based on density functional theory (controlled by ligand interaction) and found that the interaction energies are dramatically different for OA and PS (Figure S8). The DFT results suggest that interaction energy between OA films is 9 meV/formula, much lower than the interaction energy for PS films of 314 meV/formula, indicating a much stronger interaction of PS films than that of OA films. The fumaric acid is predominant on the surface of MOF and exposed to interact with other MOF NPs due to the low metal density for framework and large size of MOF NPs, which leads to low coverage of OA on the surface of MOF NPs. Thus, the interaction energy between MOF NPs was represented by calculating the organic linker fumaric acid. The resulted energy is 245 meV/formula for fumaric acid, which is close the PS film (see Table S1).

Our DFT results suggest that interactions between OA-Fe<sub>3</sub>O<sub>4</sub> NC NP and MOF NPs are hard sphere-like (9 meV/ligand is a small fraction of  $K_B T$  at room temperature). Such NPs can however experience an attraction to the interface, due to a number of mechanism.<sup>[25–28]</sup> for example, capillary liquid bridges. To determine the patterns accessible to a binary mixture of hard spheres (small: OA-Fe<sub>3</sub>O<sub>4</sub>, large: OA-MOF) with different degrees of attraction for the interface, we carried out event-driven molecular dynamics simulations (see Supporting Information). We modeled the sphere–interface interaction potential using a form linear in the distance between the sphere center and the interface. Simulations indicate that there is a crossover between a demixed configuration and a mixed configuration as we vary the ratio of the effective DEG–surface affinities,  $\alpha_{\text{large}}/\alpha_{\text{small}}$ , shown in Figure 3. In demixed configurations, the large NPs are excluded from the bottom layer, and sit on top of hexagonal lattice of small NC NPs, similar to patterns observed in experiment. On this basis we conclude that the demixed configurations seen in Figure 2a result from relatively weak NP–NP interactions combined with the absence of a strong preference for MOF–surface interactions (Figure 3b). The mixed configurations seen in experiments occur when DFT shows NP–NP interactions to be strong; we therefore attribute the mixed configurations seen in Figure 2b to strong NP–NP attractions (Figure 3c).

The experimental observations, together with theoretical modeling and simulations, demonstrate that MOFs can be controllably incorporated into self-assembled NP superstructures. Our study introduces a new method for designing multifunctional superstructures that unite both MOF and NC

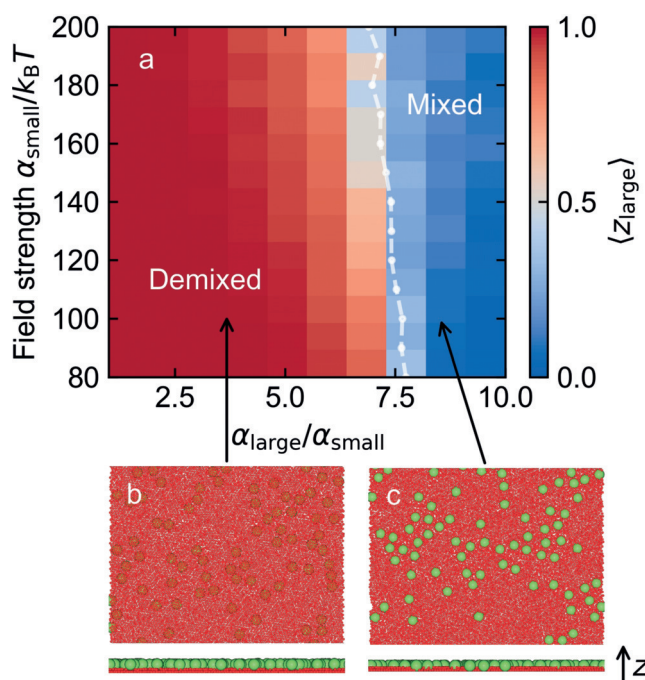


**Figure 3.** State behavior of binary hard spheres in contact with an attractive interface. a) State diagram as a function of the effective surface affinity  $\alpha$  and large: small particle affinity ratio  $\alpha_{\text{large}}/\alpha_{\text{small}}$ . The dashed line is a guide for the eye that indicates demixing.  $z_{\text{large}}$  is the distance of the large particles from the surface in units of the diameter of the small particle. b) Snapshot of the binary system in the demixed regime. Large MOF NPs (green) are on top of the hexagonal layer of Fe<sub>3</sub>O<sub>4</sub> NPs (red). c) Snapshot of the system in the mixed regime. MOF NPs penetrate the hexagonal layer of Fe<sub>3</sub>O<sub>4</sub> NPs.

materials, controlled by ligand interactions. As the MOF NPs have been demonstrated for water adsorption and Fe<sub>3</sub>O<sub>4</sub> is catalytically active, we believe these materials, which mimic supported catalyst architectures, may show promising features for catalysis and gas storage where co-localization of contrasting materials is required. In particular, it has been shown that heteromaterial combinations can leverage unique interfacial properties to realize performance enhancements, by introducing strategies such as selective intermediate (de)stabilization and activation.<sup>[29,30]</sup>

### Acknowledgements

This work was supported by the Molecular Foundry and the Advanced Light Source at Lawrence Berkeley National Laboratory, both user facilities supported by the Office of Science, Office of Basic Energy Sciences, of the U.S. Department of Energy (DOE) under Contract No. DE-AC02-05CH11231. The simulation research used resources of the National Energy Research Scientific Computing Center, a DOE Office of Science User Facility supported by the Office of Science of the U.S. Department of Energy under Contract No. DE-AC02-05CH11231. F.Q. and J.J.U. acknowledge the support by the Department of Energy through the Bay Area Photovoltaic Consortium under Award Number

DE-EE0004946. Y.F.Z. and S.D. acknowledge National Nature Science Foundation of China (No. 51325204).

### Conflict of interest

The authors declare no conflict of interest.

**Keywords:** DFT calculations · MD simulations · metal–organic frameworks · self-assembly · superstructure

**How to cite:** *Angew. Chem. Int. Ed.* **2018**, *57*, 13172–13176  
*Angew. Chem.* **2018**, *130*, 13356–13360

- [1] W. Xia, A. Mahmood, R. Q. Zou, Q. Xu, *Energy Environ. Sci.* **2015**, *8*, 1837–1866.
- [2] J. Li, Y. C. Wang, T. Zhou, H. Zhang, X. H. Sun, J. Tang, L. J. Zhang, A. M. Al-Enizi, Z. Q. Yang, G. F. Zheng, *J. Am. Chem. Soc.* **2015**, *137*, 14305–14312.
- [3] L. Y. Chen, R. Luque, Y. W. Li, *Chem. Soc. Rev.* **2017**, *46*, 4614–4630.
- [4] J. H. Choi, A. T. Fafarman, S. J. Oh, D. K. Ko, D. K. Kim, B. T. Diroll, S. Muramoto, J. G. Gillen, C. B. Murray, C. R. Kagan, *Nano Lett.* **2012**, *12*, 2631–2638.
- [5] E. V. Shevchenko, M. Ringler, A. Schwemer, D. V. Talapin, T. A. Klar, A. L. Rogach, J. Feldmann, A. P. Alivisatos, *J. Am. Chem. Soc.* **2008**, *130*, 3274–3275.
- [6] Y. J. Kang, X. C. Ye, J. Chen, Y. Cai, R. E. Diaz, R. R. Adzic, E. A. Stach, C. B. Murray, *J. Am. Chem. Soc.* **2013**, *135*, 42–45.
- [7] O. Chen, L. Riedemann, F. Etoc, H. Herrmann, M. Coppey, M. Barch, C. T. Farrar, J. Zhao, O. T. Bruns, H. Wei, P. Guo, J. Cui, R. Jensen, Y. Chen, D. K. Harris, J. M. Cordero, Z. W. Wang, A. Jasanoff, D. Fukumura, R. Reimer, M. Dahan, R. K. Jain, M. G. Bawendi, *Nat. Commun.* **2014**, *5*, 5093–5015.
- [8] X. C. Ye, J. Y. Fei, B. T. Diroll, T. Paik, C. B. Murray, *J. Am. Chem. Soc.* **2014**, *136*, 11680–11686.
- [9] X. C. Ye, J. Chen, B. T. Diroll, C. B. Murray, *Nano Lett.* **2013**, *13*, 1291–1297.
- [10] J. J. Urban, D. V. Talapin, E. V. Shevchenko, C. R. Kagan, C. B. Murray, *Nat. Mater.* **2007**, *6*, 115–121.
- [11] J. J. Urban, D. V. Talapin, E. V. Shevchenko, C. B. Murray, *J. Am. Chem. Soc.* **2006**, *128*, 3248–3255.
- [12] E. V. Shevchenko, D. V. Talapin, N. A. Kotov, S. O'Brien, C. B. Murray, *Nature* **2006**, *439*, 55–59.
- [13] R. Tan, H. Zhu, C. Cao, O. Chen, *Nanoscale* **2016**, *8*, 9944–9961.
- [14] E. V. Shevchenko, D. V. Talapin, C. B. Murray, S. O'Brien, *J. Am. Chem. Soc.* **2006**, *128*, 3620–3637.
- [15] J. J. Wei, N. Schaeffer, M. P. Pileni, *J. Am. Chem. Soc.* **2015**, *137*, 14773–14784.
- [16] B. W. Goodfellow, Y. X. Yu, C. A. Bosoy, D. M. Smilgies, B. A. Korgel, *J. Phys. Chem. Lett.* **2015**, *6*, 2406–2412.
- [17] H. Xiong, D. van der Lelie, O. Gang, *J. Am. Chem. Soc.* **2008**, *130*, 2442–2443.
- [18] J. O. Kim, K. I. Min, H. Noh, D. H. Kim, S. Y. Park, D. P. Kim, *Angew. Chem. Int. Ed.* **2016**, *55*, 7116–7120; *Angew. Chem.* **2016**, *128*, 7232–7236.
- [19] K. Na, K. M. Choi, O. M. Yaghi, G. A. Somorjai, *Nano Lett.* **2014**, *14*, 5979–5983.
- [20] H. Furukawa, F. Gandara, Y. B. Zhang, J. Jiang, W. L. Queen, M. R. Hudson, O. M. Yaghi, *J. Am. Chem. Soc.* **2014**, *136*, 4369–4381.
- [21] A. M. Fracaroli, H. Furukawa, M. Suzuki, M. Dodd, S. Okajima, F. Gandara, J. A. Reimer, O. M. Yaghi, *J. Am. Chem. Soc.* **2014**, *136*, 8863–8866.
- [22] S. S. Kaye, A. Dailly, O. M. Yaghi, J. R. Long, *J. Am. Chem. Soc.* **2007**, *129*, 14176–14177.
- [23] L. Yu, Y. Liu, F. Yang, J. Evans, J. A. Rodriguez, P. Liu, *J. Phys. Chem. C* **2015**, *119*, 16614–16622.
- [24] A. G. Dong, J. Chen, P. M. Vora, J. M. Kikkawa, C. B. Murray, *Nature* **2010**, *466*, 474–477.
- [25] H. T. Dobbs, G. A. Darbellay, J. M. Yeomans, *Europhys. Lett.* **1992**, *18*, 439.
- [26] E. Rabani, D. R. Reichman, P. L. Geissler, L. E. Brus, *Nature* **2003**, *426*, 271.
- [27] A. Böker, J. He, T. Emrick, T. P. Russell, *Soft Matter* **2007**, *3*, 1231–1248.
- [28] F. Bresme, M. Oettel, *J. Phys. Condens. Matter* **2007**, *19*, 413101.
- [29] B. Rungtaweeworanit, J. Baek, J. R. Araujo, B. S. Archanjo, K. M. Choi, O. M. Yaghi, G. A. Somotjai, *Nano Lett.* **2016**, *16*, 7645–7649.
- [30] Z. M. Cui, G. T. Fu, Y. T. Li, J. B. Goodenough, *Angew. Chem. Int. Ed.* **2017**, *56*, 9901–9905; *Angew. Chem.* **2017**, *129*, 10033–10037.

Manuscript received: July 7, 2018  
Revised manuscript received: August 12, 2018  
Accepted manuscript online: August 22, 2018  
Version of record online: September 11, 2018